

Supplementary Materials:  
High interseismic coupling in the Eastern Makran  
(Pakistan) subduction zone.

N. Y. Lin<sup>a</sup>, R. Jolivet<sup>a,e</sup>, M. Simons<sup>a</sup>, P. S. Agram<sup>b</sup>, H. R. Martens<sup>a</sup>, Z. Li<sup>c</sup>,  
S. H. Lodi<sup>d</sup>

<sup>a</sup>*Seismological Laboratory, Geological and Planetary Sciences, California Institute of Technology, 1200 E California Blvd, Pasadena, CA 91125, USA.*

<sup>b</sup>*Jet Propulsion Laboratory, California Institute of Technology, 4800 Oak Grove Drive, Pasadena, California 91109, USA.*

<sup>c</sup>*COMET, School of Civil Engineering and Geosciences, Newcastle University, Newcastle upon Tyne, NE1 7RU, United Kingdom.*

<sup>d</sup>*Department of Civil Engineering, NED University of Engineering and Technology, Karachi 75270, Pakistan.*

<sup>e</sup>*now at COMET, Bullard Labs, Department of Earth Sciences, University of Cambridge, Madingley Road, CB3 0EZ, Cambridge, UK.*

## 1. InSAR Processing

In this section, we show additional figures about the processing of the InSAR data. Supplementary materials also include geocoded line-of-sight velocity maps and corresponding maps of the line-of-sight vector in GRD format. For each track, the file `_Mints_Velocity.grd` contains the line-of-sight velocity of the ground in cm/yr, the file `_Mints_Error.grd` contains the uncertainty along the line-of-sight in cm/yr and the files `_Incidence_East.grd`, `_Incidence_North.grd` and `_Incidence_Up.grd` contains the East, North and Up components of the line-of-sight vector at each pixel. The files can be downloaded at:

### 1.1. InSAR data set

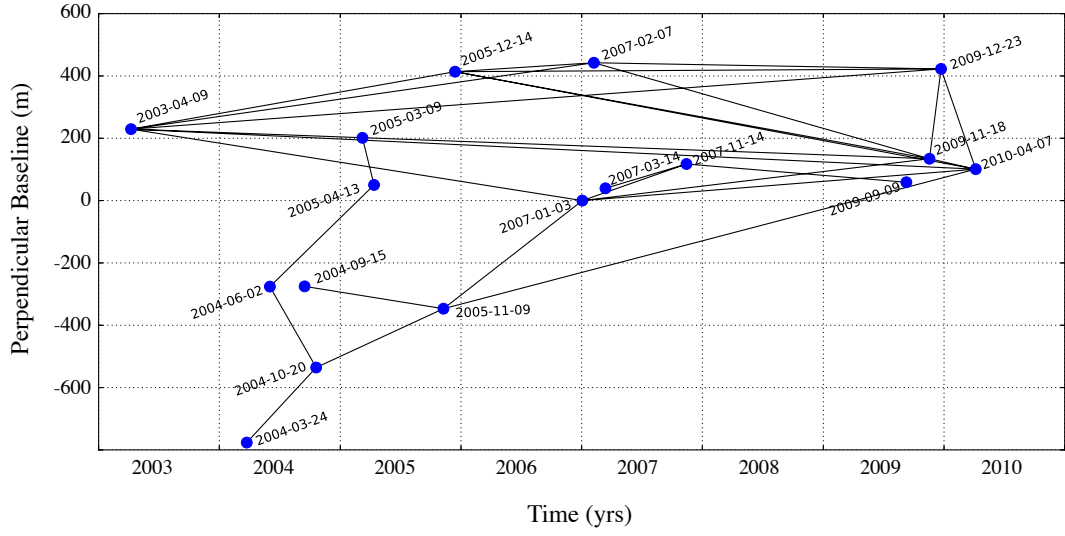


Figure S-1: **Baseline plot of Track 220** - Plot of the perpendicular baseline of SAR acquisitions as a function of time along Envisat track 220. Blue dots are acquisitions and black lines indicate the interferograms formed by combination of these acquisitions.

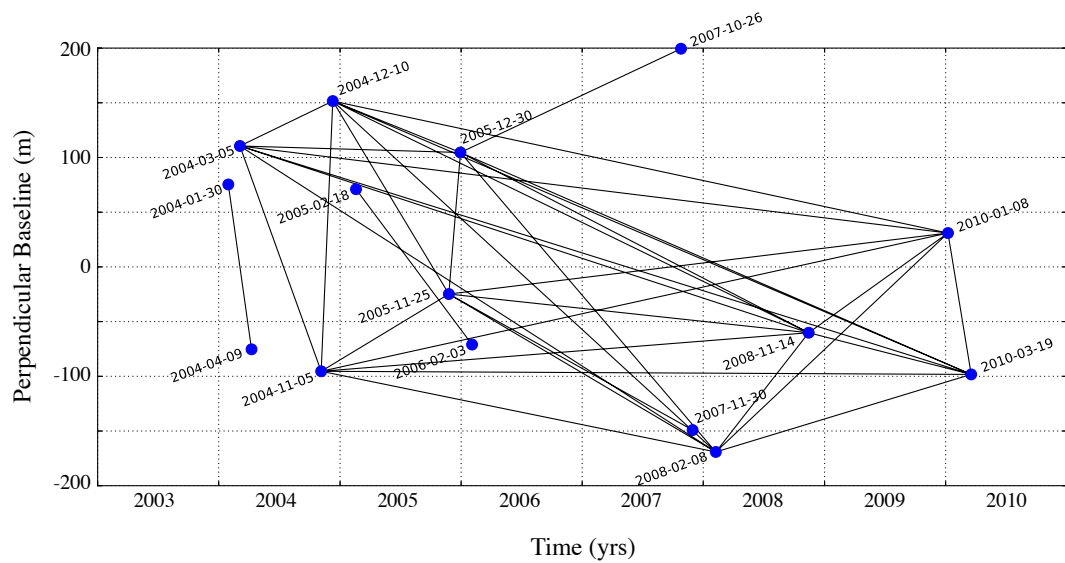


Figure S-2: **Baseline plot of Track 449** - Plot of the perpendicular baseline of SAR acquisitions as a function of time along Envisat track 449. Blue dots are acquisitions and black lines indicate the interferograms formed by combination of these acquisitions.



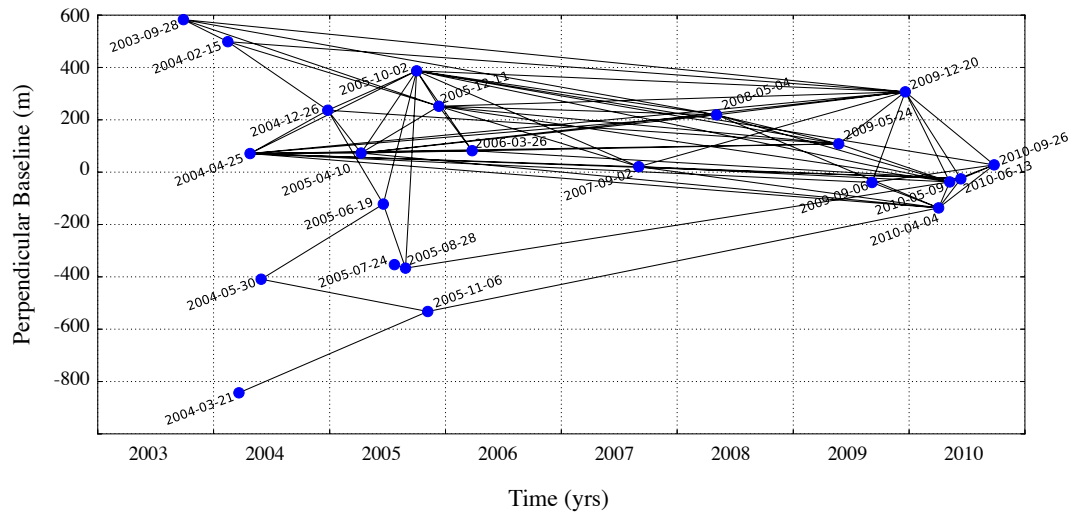


Figure S-3: **Baseline plot of Track 177** - Plot of the perpendicular baseline of SAR acquisitions as a function of time along Envisat track 177. Blue dots are acquisitions and black lines indicate the interferograms formed by combination of these acquisitions.

## 1.2. Atmospheric and Tidal Corrections

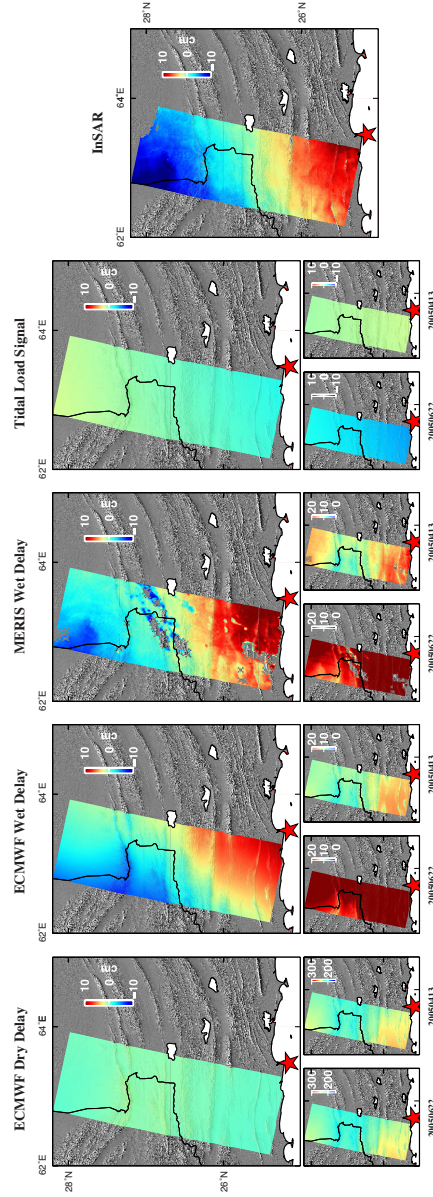


Figure S-4: **Example of cumulative corrections for InSAR**

Figure S-4: **Example of cumulative corrections for InSAR - From Left to Right:** Synthetic interferometric phase delay between Envisat ASAR acquisitions on June 22nd, 2005 and April 13th, 2005. Predictions have been computed to model the hydrostatic and wet delays using input from ECMWF's ERA-Interim, the wet delay using input from Medium Resolution Imaging Spectrometer (MERIS) and the tidal load signal using inputs from the oceanic model FES2004. We correct the original interferogram (far right) by combining the hydrostatic delay from ECMWF, the wet delay from MERIS and the tidal load signal. More details on the correction method can be found in Jolivet et al. (2014).

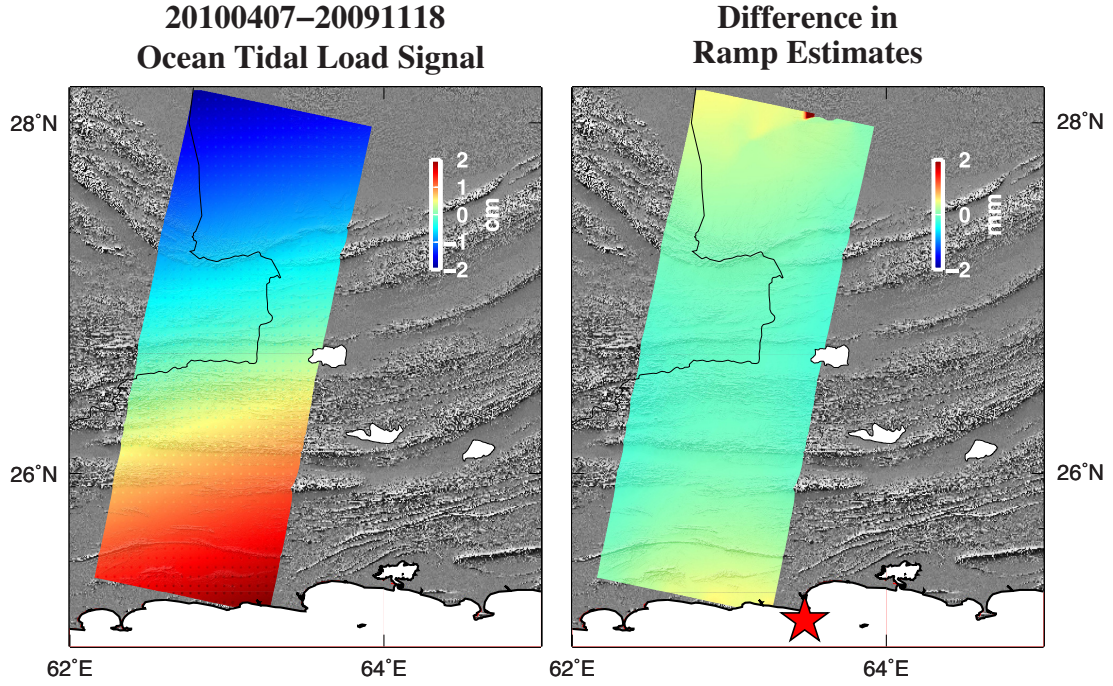


Figure S-5: **Effect of the ocean tidal load signal on the long wavelength field** - **Left:** Prediction of the oceanic tidal load signal for the interferogram combining Envisat acquisitions on November 18th, 2009 and April 7th, 2011. Tidal constituents from the FES2004 tidal model are M2, S2, N2, O1, P1, Q1, S1, K1, M4, MF and MM. **Right:** Difference in estimated orbital ramp on interferogram with and without the signal of the oceanic tidal load. The orbital ramp is modeled as a linear function of range and azimuth. Correcting from OTL signals allows to better estimate the long wavelength of the deformation field (Jolivet et al., 2014).

### 1.3. Comparison of velocity maps

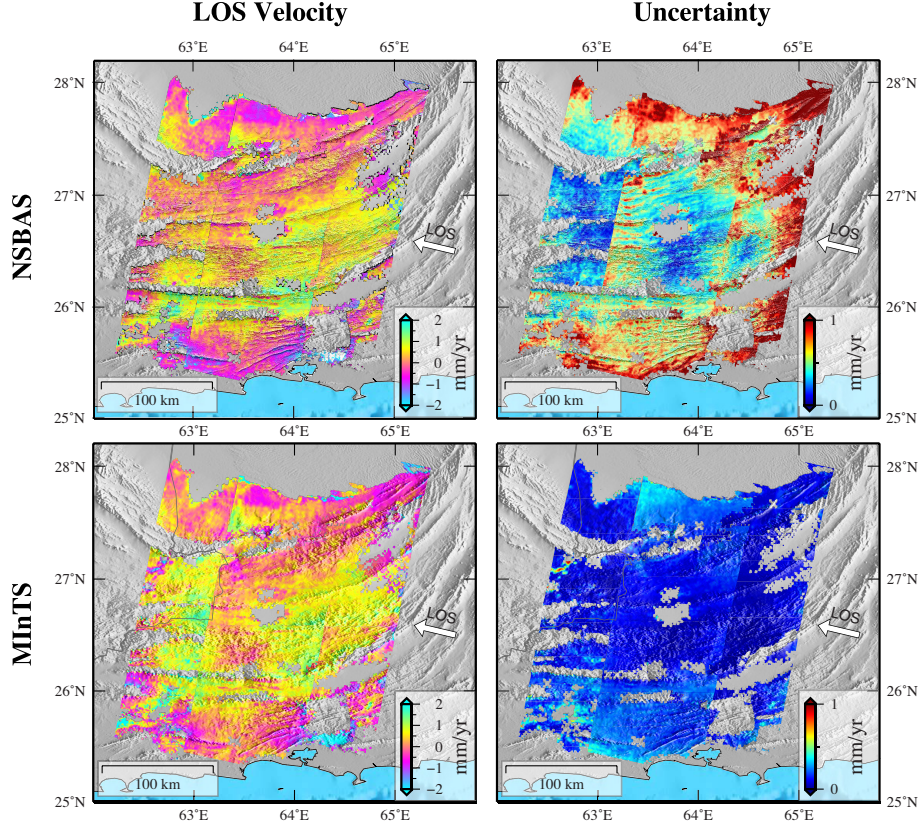


Figure S-6: **Line-Of-Sight velocity maps - Left** Maps of the Line-Of-Sight (LOS) velocity along Envisat tracks 220, 449 and 177 derived using the New Small Baseline Subset method (NSBAS; top row) and the Multiscale Interferometric Time Series method (MInTS; bottom row) (see Fig. 1 in the main text for the respective positions of Envisat tracks). White arrow indicates the LOS pointing from the satellite. Positive velocity is toward satellite. **Right** Maps of uncertainty on the LOS velocity derived using the NSBAS method (top row) and the MInTS method (bottom row) along Envisat tracks 220, 449 and 177.

## **2. Comparing the effect of different azimuth of plate convergence on the inferred geodetic coupling**

As we use the back-slip formulation to invert for the degree of fault locking that explains our dataset, we need to assume the azimuth of convergence of the Arabia plate with respect to Eurasia. Following the recent recognition of the Ormara micro plate, that has no emerged land, the convergence is not fully constrained. For our preferred model, we use a  $10^{\circ}\text{N}$  azimuth of convergence as it fits with both estimates from geodesy and geology (see references in Fig. S-7). However, some discussion is needed about the effect of a variable convergence azimuth.

Although very few data were available to constrain the focal mechanism, the slip vector of the 1945 M8 Makran earthquake shows a  $20\text{-}25^{\circ}\text{W}$  azimuth (Byrne et al., 1992). In addition, the analysis of significant earthquakes ( $M > 5$ ) over the 2004-2012 period on the megathrust reveals a large range of slip vector azimuths Ekström et al. (2012). Therefore, we test models with a different azimuths of convergence,  $8^{\circ}\text{W}$  and north. We apply the same methodology as presented in the main text. For each of the these test, the models do not fit the data as well as our preferred orientation and do not predict at all the few GPS velocities available in the region (see Figure S-8 for the  $8^{\circ}\text{W}$  azimuth of convergence and Figure S-9 for a North oriented convergence).

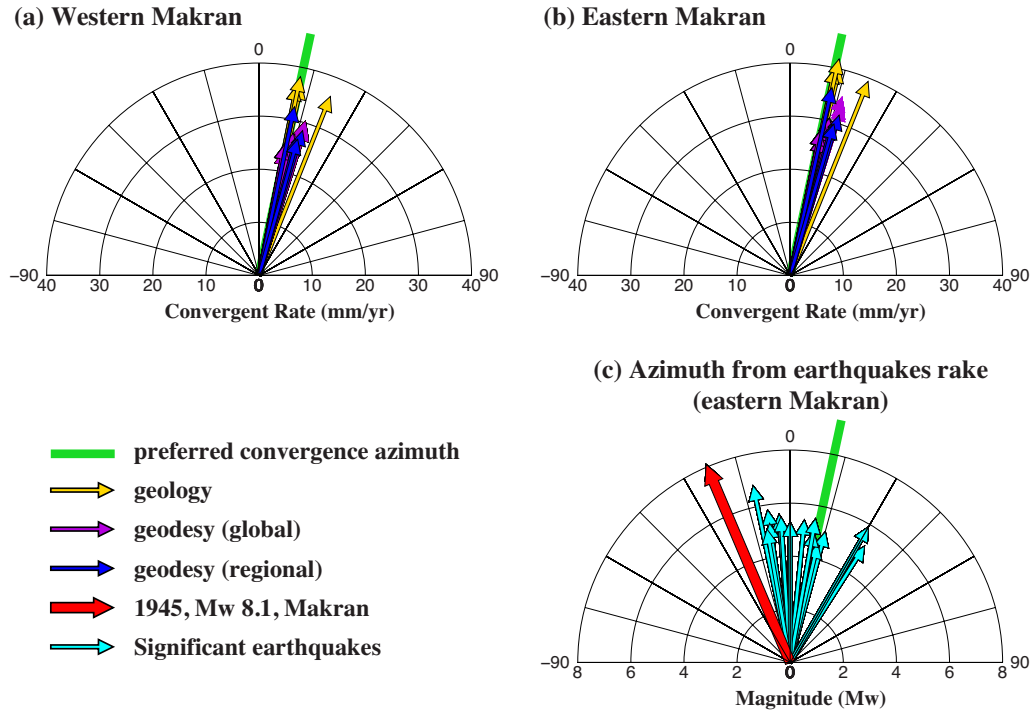


Figure S-7: **Azimuth of plate convergence from geology, geodesy and seismology** - **a.** Azimuths and rates of convergence derived from geological and geodetic studies for western Makran (i.e. west of the Sistan Suture Zone). **b.** Azimuths and rates of convergence from geological and geodetic studies for eastern Makran. **c.** Azimuths and moment magnitude extracted from significant thrust earthquakes (source: Global CMT catalog, Ekström et al. (2012) and Byrne et al. (1992)). The direction of convergence used in our preferred model is indicated in **a.**, **b.** and **c.** by a thick green line. References for **a.** and **b.** include: Gripp and Gordon (1990); Argus and Gordon (1991); DeMets et al. (1994); Drewes (1998); S McClusky (2000); Drewes and Angermann (2001); Gripp and Gordon (2002); Sella et al. (2002); Kreemer et al. (2003); McClusky et al. (2003); Prawirodirdjo and Bock (2004); Vernant et al. (2004); Reilinger et al. (2006); Drewes (2009); Argus et al. (2010); DeMets et al. (2010).



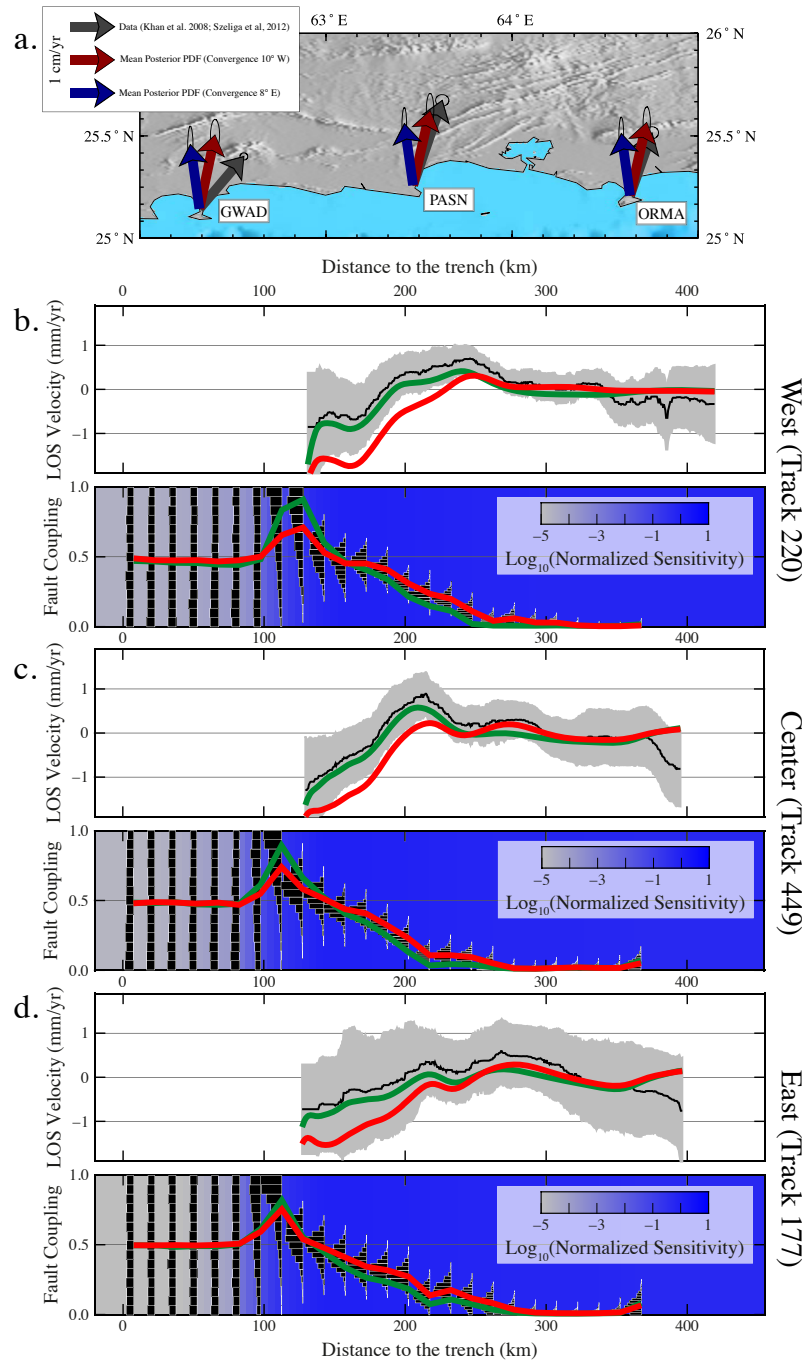


Figure S-8: Coupling inferred using a 8°W azimuth of convergence of the Arabia plate - See next page for caption



Figure S-8: **Coupling inferred using a 8°W convergence azimuth of the Arabia plate -** **a.** Gray arrows are GPS velocities along the coast of eastern Makran with their associated uncertainties. Red arrows are the predictions from the mean posterior PDF of fault coupling estimated with a 10°E azimuth of convergence (see main text). Blue arrows are predictions from the mean posterior PDF of fault coupling estimated with a 8°W azimuth of convergence. **b.** Top: Trench-perpendicular profile of the LOS velocity inferred from data on Envisat track 220 (black line) and the associated standard deviation (gray shading). Red line is the prediction from the mean posterior PDF of fault coupling when including estimates of the prediction error,  $C_p$ . Green line is the prediction from the mean posterior PDF of fault coupling without including  $C_p$ . Bottom: Posterior PDFs (black boxes), mean of the posterior PDF (red line) and mean of the posterior PDF without accounting for  $C_p$  (green line) of fault coupling inferred from the profile of LOS velocity on track 220. Background color is the sensitivity (see main text). **c.** Same as **b.** with the data from track 449. **d.** Same as **b.** with data from track 177.

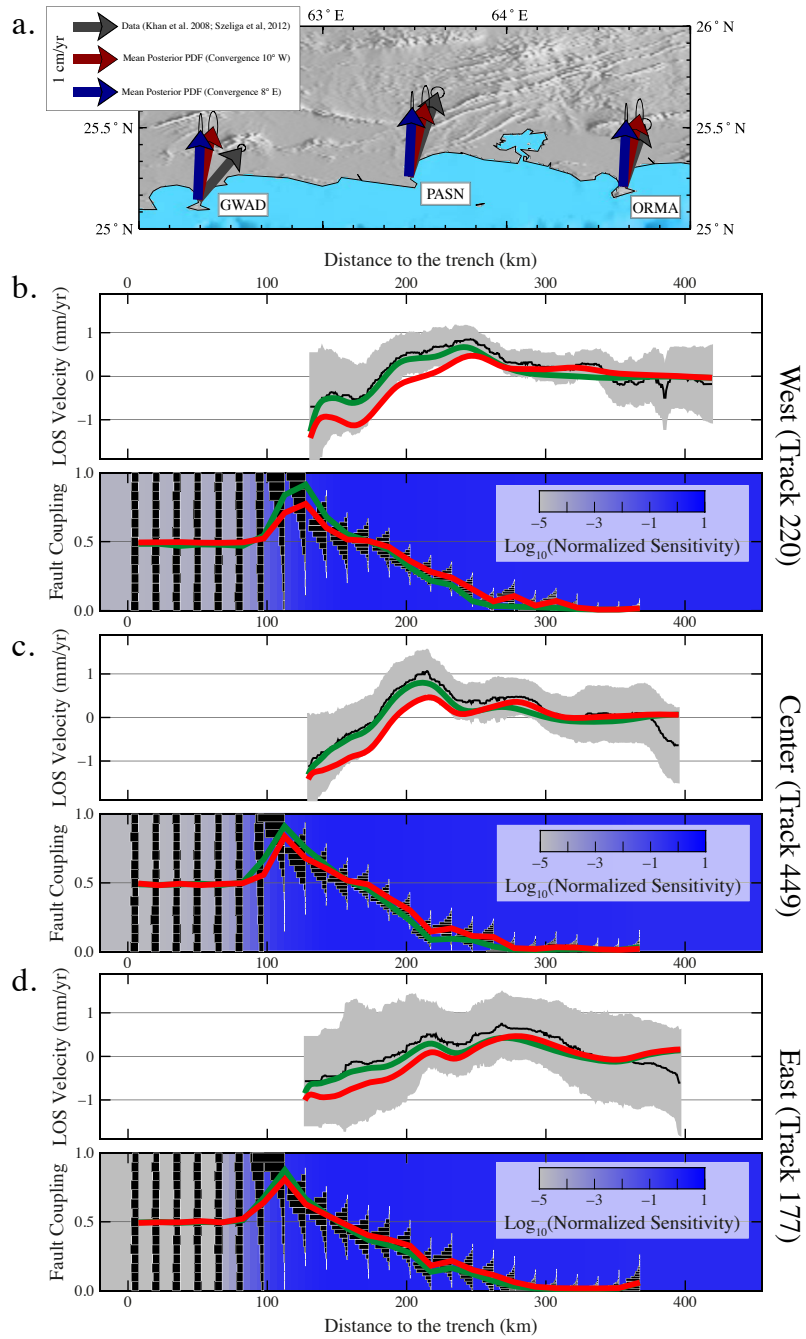


Figure S-9: **Coupling inferred using straight north convergence of the Arabia plate** - See next page for caption

Figure S-9: **Coupling inferred using a straight north convergence of the Arabia plate** - **a.** Gray arrows are GPS velocities along the coast of eastern Makran with their associated uncertainties. Red arrows are the predictions from the mean posterior PDF of fault coupling estimated with a  $10^\circ\text{E}$  azimuth of convergence (see main text). Blue arrows are predictions from the mean posterior PDF of fault coupling estimated with straight north convergence. **b.** Top: Trench-perpendicular profile of the LOS velocity inferred from data on Envisat track 220 (black line) and the associated standard deviation (gray shading). Red line is the prediction from the mean posterior PDF of fault coupling when including estimates of the prediction error,  $\mathbf{C}_p$ . Green line is the prediction from the mean posterior PDF of fault coupling without including  $\mathbf{C}_p$ . Bottom: Posterior PDFs (black boxes), mean of the posterior PDF (red line) and mean of the posterior PDF without accounting for  $\mathbf{C}_p$  (green line) of fault coupling inferred from the profile of LOS velocity on track 220. Background color is the sensitivity (see main text). **c.** Same as **b.** with the data from track 449. **d.** Same as **b.** with data from track 177.

### 3. Effect of along-strike variations of the along-dip width of the coupled zone.

In the main text, we invoke the possibility that variations of the width of the coupled zone may be a possibility to explain the azimuth of the velocity measured at the site GWAD. Indeed, given the elastic response of the ground to slip on a patch embedded in an elastic half-space (stratified or homogeneous), a station located above a creeping patch, next to a locked patch, will be “dragged” toward the locked patch. We illustrate this possibility using a simple forward 3D model of the subduction. The geometry of the fault follows the megathrust geometry defined by Byrne et al. (1992). We discretize the fault in  $10 \times 15$  km patches, with infinitely long patches on the edges, to avoid edge effects. The response to slip on each patch is computed using a layered elastic half-space, using the same characteristics as described in the main text. We construct a synthetic distribution of coupling that fits, to first order, with the available GPS velocities (Fig. S-10).

In our toy model, coupling is enforced to follow a gaussian function of the distance to the trench. Maximum coupling is 1, while minimum is 0. The characteristic width of the gaussian varies along-strike: (1) between the easternmost edge of the model and the limit indicated in blue in figure S-10, the width of the gaussian is of 50 km, (2) from the limit, to the westernmost edge of the model, the width of the gaussian decreases linearly to 10 km. This configuration results in a dual distribution of coupling with a large region with high coupling (0.8 to 1.0) to the east and a smaller region with intermediate coupling to the west.

We compute the velocities at the stations ORMA, PASN and GWAD

and on regularly spaced position in the vicinity of these stations. Although we do not fit completely the GPS velocities, which is expected as we do not optimise the solution, the predicted velocity field shows a variation in the azimuth of the predicted ground velocities, from  $10^{\circ}\text{N}$  to the east (i.e. parallel to the azimuth of convergence imposed) to  $21^{\circ}\text{N}$ . An infinitely long fault with constant coupling would predict parallel velocity vectors, with a  $10^{\circ}\text{N}$  azimuth. Such three-dimensional effect could therefore explain the variation in azimuth of the velocity at site GWAD.

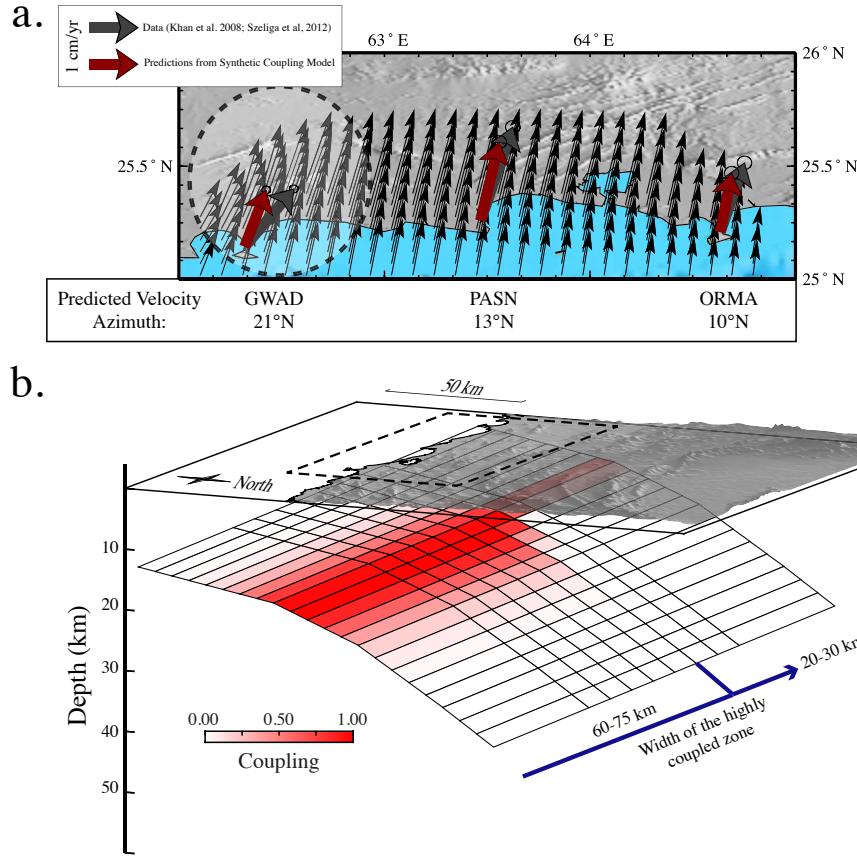


Figure S-10: **Variation of the azimuth of predicted velocities due to along-strike variations of coupling** - **a.** Black arrows are GPS velocities at equally sampled locations predicted by the coupling model in **b.**. Thick grey arrows are GPS velocities measured by Khan et al. (2008) and Szeliga et al. (2012). Dark red arrows are velocities predicted by the coupling model shown in **b.** Background shading is topography from SRTM. White shading indicates the area where predicted GPS velocities deviates significantly from the 10°N azimuth expected. **b.** 3-D view of the synthetic coupling model used to explore the effect of along-strike variations of coupling. Dashed line at the surface indicates the area covered in **a.**

## References

- Argus, D. F., Gordon, R. G., 1991. No-net-rotation model for current plate velocities in incorporating plate model model NUVEL-1. *Geophys. Res. Lett.* 18 (11), 2039–2042.
- Argus, D. F., Gordon, R. G., Heflin, M. B., Ma, C., Eanes, R. J., Willis, P., Peltier, W. R., Owen, S. E., 2010. The angular velocities of the plates and the velocity of Earth’s centre from space geodesy. *Geophys. J. Int.* 180 (3), 913–960.
- Byrne, D. E., Sykes, L. R., Davis, D. M., 1992. Great thrust earthquakes and aseismic slip along the plate boundary of the Makran Subduction Zone. *J. Geophys. Res.* 97 (B1), 449–478.
- DeMets, C., Gordon, R. G., Argus, D. F., 2010. Geodetically current plate motions. *Geophys. J. Int.* 181 (1), 1–80.
- DeMets, C., Gordon, R. G., Argus, D. F., Stein, S., 1994. Effect of recent revisions to the geomagnetic reversal time scale on estimates of current plate motions. *Geophys. Res. Lett.* 21 (20), 2191–2194.
- Drewes, H., Angermann, D., 2001. The actual plate kinematic and crustal deformation model 2000 (apkim2000) as a geodetic reference system. In: AIG 2001 Scientific Assembly, Budapest.
- Drewes, H., 1998. Combination of VLBI, SLR and GPS determined station velocities for actual plate kinematic and crustal deformation models. In: *Geodynamics*. M. Feissel, Springer.
- Drewes, H., 2009. *Geodetic Reference Frames*. Springer, Ch. The actual plate kinematic and crustal deformation model APKIM2005 as basis for a non-rotating ITRF, pp. 95–99.

- Ekström, G., Nettles, M., Dziewonski, A. M., 2012. The global CMT project 2004–2010: Centroid-moment tensors for 13,017 earthquakes. *Phys. Earth Planet. Inter.* 200, 1–9.
- Gripp, A. E., Gordon, R. G., 1990. Current plate velocities relative to the hotspots in incorporating the NUVEL-1 global plate motion model. *Geophys. Res. Lett.* 17 (8), 1109–1112.
- Gripp, A. E., Gordon, R. G., 2002. Young tracks of hotspots and current plate velocities. *Geophys. J. Int.* 150 (2), 321–361.
- Jolivet, R., Agram, P. S., Lin, N. Y., Simons, M., Doin, M.-P., Peltzer, G., Li, Z., 2014. Improving InSAR geodesy using Global Atmospheric Models. *J. Geophys. Res.* 119, B010588.
- Khan, M. A., Bendick, R., Bhat, M. I., Bilham, R., Kakar, D. M., Khan, S. F., Lodi, S. H., Qazi, M. S., Singh, B., Szeliga, W., A, W., 2008. Preliminary geodetic constraints on plate boundary deformation on the western edge of the Indian plate from TriGGnet (Tri-University GPS Geodesy Network). *J. Him. Earth Sci.* 41, 71–87.
- Kreemer, C., Holt, W. E., Haines, A. J., 2003. An integrated global model of present-day plate motions and plate boundary deformation. *Geophys. J. Int.* 154 (1), 8–34.
- McClusky, S. et al, 2000. Global Positioning System constraints on plate kinematics and dynamics in the eastern Mediterranean and Caucasus. *J. Geophys. Res.*, 105 (B3), 5695–5719.
- McClusky, S., Reilinger, R., Mahmoud, S., Ben Sari, D., Tealeb, A., 2003. GPS



- constraints on Africa (Nubia) and Arabia plate motions. *Geophys. J. Int.*, 155 (1), 126–138.
- Prawirodirdjo, L., Bock, Y., 2004. Instantaneous global plate motion model from 12 years of continuous GPS observations. *J. Geophys. Res.* 109 (B8).
- Reilinger, R., McClusky, S., Vernant, P., Lawrence, S., Ergintav, S., Cakmak, R., Ozener, H., Kadirov, F., Guliev, I., Stepanyan, R., Nadariya, M., Hahubia, G., Mahmoud, S., Sakr, K., ArRajehi, A., Paradissis, D., Al-Aydrus, A., Prilepin, M., Guseva, T., Evren, E., Dmitrotsa, A., Filikov, S. V., Gomez, F., Al-Ghazzi, R., Karam, G., 2006. GPS constraints on continental deformation in the Africa-Arabia-Eurasia continental collision zone and implications for the dynamics of plate interactions. *J. Geophys. Res.* 111 (B5), B05411.
- Sella, G. F., Dixon, T. H., Mao, A. L., 2002. REVEL: A model for Recent plate velocities from space geodesy. *J. Geophys. Res.* 107 (B4).
- Szeliga, W., Bilham, R., Kakar, D. M., Lodi, S. H., 2012. Interseismic strain accumulation along the western boundary of the Indian subcontinent. *J. Geophys. Res.* 117 (B8), B08404.
- Vernant, P., Nilforoushan, F., Hatzfeld, D., Abbassi, M. R., Vigny, C., Masson, F., Nankali, H., Martinod, J., Ashtiani, A., Bayer, R., Tavakoli, F., CHERY, J., 2004. Present-day crustal deformation and plate kinematics in the Middle East constrained by GPS measurements in Iran and northern Oman. *Geophys. J. Int.* 157 (1), 381–398.